

Mineral magnetic variation of the minle loess/palaeosol sequence of the late glacial to holocene period in the northeastern Tibetan Plateau

Jianguo Xiong,^{1,2,3} Yuezhi Zhong^{1b, 3,4}, Caicai Liu^{1b, 1}, Qingri Liu,^{1,3} Huiping Zhang,¹ Chenglong Deng⁵ and Youli Li³

¹State Key Laboratory of Earthquake Dynamics, Institute of Geology, China Earthquake Administration, Beijing 100029, China

²Guangdong Provincial Key Laboratory of Geodynamics and Geohazards, School of Earth Science and Engineering, Sun Yat-sen University, Guangzhou 510275, China

³Key Laboratory of Earth Surface Processes of Ministry of Education, Peking University, Beijing 100871, China. E-mail: 1401214641@pku.edu.cn

⁴Department of Earth Sciences, ETH Zurich, Zurich 8092, Switzerland

⁵State Key Laboratory of Lithospheric Evolution, Institute of Geology and Geophysics, Chinese Academy of Sciences, Beijing 100029, China.

Accepted 2023 July 24. Received 2023 July 10; in original form 2023 June 15

SUMMARY

Located at the modern junction of the Asian Summer Monsoon and the Westerlies, the northeastern Tibetan Plateau and western Chinese Loess Plateau are in distinct climatic setting from the middle and eastern Chinese Loess Plateau. Besides, Holocene climate variations near the Asian Summer Monsoon margin are highly debated with different models proposed. We carried out environmental magnetic analyses on the Minle loess section, with continuous deposition between 13.3–0.5 ka, located near this margin. Results show that the magnetic susceptibilities of palaeosols are dominantly contributed by superparamagnetic (SP) and single-domain (SD) maghemite and/or magnetite produced by pedogenesis. Limited changes in the content of haematite indicate that dust origin hardly influenced the magnetic mineral variations. The section is divided into four substages according to the changes in magnetic indices and provides a full scene of Holocene climatic evolutions. During the coldest and driest Late Glacial (13.3–11.7 ka), it displays the weakest pedogenesis, as suggested by the lowest SP and SD concentration. The strongest pedogenesis in the Minle section produced higher magnetic susceptibility than the loess records in the Chinese Loess Plateau during the early Holocene Optimum (11.7–8.1 ka). The subsequently declined summer insolation, equatorward migrated Westerlies and the weakened Asian Summer Monsoon led to weak pedogenesis during the middle Holocene (8.1–5.3 ka). Stronger pedogenesis during the late Holocene (5.3–0.5 ka) than the middle Holocene might be due to lower evapotranspiration from weaker insolation and/or to the enhanced winter Westerlies. We attribute the spatiotemporal differences in climatic records of the Chinese loess to precipitation, effective humidity and aeolian geomorphological processes.

Key words: Geomorphology; Environmental magnetism; Tectonics and climatic interactions; Holocene; Chinese Loess Plateau.

1 INTRODUCTION

Since the late Cenozoic, the arid Gobi and deserts in northwestern China have provided continuous dust accumulation for the formation of the Chinese Loess Plateau (Fig. 1). The loess–palaeosol (PL–PS) sequences contain essentially continuous magnetic and palaeoclimate records from the Miocene (e.g. Heller & Liu 1984; An *et al.* 2001; Guo *et al.* 2002). Many environmental proxies have been used to reconstruct the evolution history of the palaeomonsoon in East Asia since the late Cenozoic. Environmental magnetism of

loess deposits plays an indispensable role in reconstructing the history of monsoon variation and aridification (Heller & Liu 1984; Zhou *et al.* 1990; Maher & Thompson 1992; Forster & Heller 1997; Barrón & Torrent 2002; Jiang *et al.* 2022). However, the palaeoenvironmental factors in different regions lead to complicated mechanisms of loess magnetism and its variations. For example, in the central Chinese Loess Plateau, the precipitation under the control of the East Asian Summer Monsoon was considered as the primary factor that increased much finer superparamagnetic (SP) and single-domain (SD) magnetite/magnetite grains in PS layers than in loess

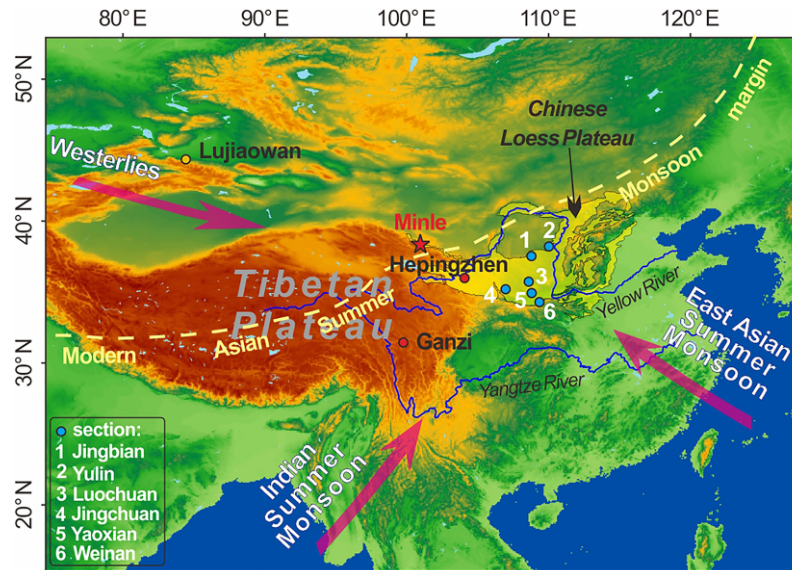


Figure 1. Map showing the location of the Minle section (denoted by the red star), and the dominant circulation systems (arrows) including the Westerlies and Asian Summer Monsoon (containing the East Asian Summer Monsoon and Indian Summer Monsoon). The modern Asian Summer Monsoon limit (Chen *et al.* 2010, and references therein) is shown by a dashed line. Solid cycles represent loess sections, and please see Fig. 10 for their climatic records.

layers, resulting in significant differences in their magnetic susceptibilities (e.g. Deng *et al.* 2005, 2006; Liu *et al.* 2007). In contrast, under the influence of the interaction of the Indian Monsoon and Westerlies, the Ganzi loess section in the eastern Tibetan Plateau shows enhanced magnetism in PS layers controlled by the soil water balance, which is maintained by precipitation and evapotranspiration (Fig. 1, Hu *et al.* 2015). Nevertheless, its magnetism is weaker than the Luochuan loess (Hu *et al.* 2015).

The northeastern Tibetan Plateau is close to the deserts in north-western China, the main dust provenance areas. This area preserves continuous loess deposits (Li *et al.* 2022b; Zhong *et al.* 2022) and constitutes an important part of the western Chinese Loess Plateau. It is controlled by the interaction between the Asian Monsoon and the Westerlies (An *et al.* 2012; Li *et al.* 2022b), while the central Chinese Loess Plateau and the southeastern Tibetan Plateau are controlled by the Asian Monsoon. Environmental magnetic investigations have been widely conducted on the loess deposits in the central Chinese Loess Plateau, but there are much fewer on the western margin of the Chinese Loess Plateau. Identifying and quantifying the magnetic minerals of loess in this region and understanding the specific environment in which they were formed will help understand the environmental magnetism in different regions.

The Holocene climate changes in the northeastern Tibetan Plateau are highly debated. For example, an early (Chen *et al.* 2006; Hartmann & Wünnemann 2009; Zhang & Li 2016; Zhong *et al.* 2022) or middle (Herzschuh *et al.* 2004; Yu *et al.* 2006; Li *et al.* 2009a,b) Holocene climatic optimum was suggested. Different models on the Holocene climate changes on millennial to centennial scales were also proposed: (1) the wettest early Holocene and gradually drying middle-late Holocene (Hartmann & Wünnemann 2009; Zhang & Li 2016); (2) the wet early and late Holocene, but dry middle Holocene (Chen *et al.* 2006); (3) the wet early-middle Holocene, but dry late Holocene (Yu *et al.* 2006; Wünnemann *et al.* 2007) and (4) the wettest middle Holocene but the driest late Holocene (Li *et al.* 2009a,b; Long *et al.* 2010, 2012).

Reasons for these debates are multifold, and the temporal resolution and reliability of climatic proxies measured from sedimentary records are two possible factors. In this paper, we undertook a mineral magnetic study on the Minle loess section, located at the mountain front in the northeastern Tibetan Plateau. This section has recorded the climate change of the northeastern Tibetan Plateau on the centennial scale since the Last Deglacial (Zhong *et al.* 2022). Therefore, the Minle section provides a valuable opportunity to quantify the assemblage of pedogenic magnetic minerals and the climate changes indicated by them on the western margin of the Chinese Loess Plateau. Specifically, mineral magnetism, including high-temperature magnetic susceptibilities ($\chi-T$ curves), hysteresis properties, first-order reversal curve (FORC) diagrams, anhysteretic remanent magnetization (ARM), saturation isothermal remanent magnetization (SIRM) and the diffuse reflectance spectroscopy (DRS) analysis were carried out. We attempted to provide robust evidence from environmental magnetism of the Minle section to settle these controversies, and to discuss the spatiotemporal differences and their influencing factors in climate change recorded by loess in China.

2 GEOLOGICAL SETTING

The Minle loess section ($38^{\circ}15'59.00''\text{N}$ $100^{\circ}52'36.86''\text{E}$, 2766 m above sea level) is located in the north piedmont of the Qilian Shan in the northeastern Tibetan Plateau (Fig. 1). It also belongs to the western extension of the Chinese Loess Plateau. The mountain front shows a typical steppe-meadow landscape with a modern mean annual temperature of $\sim 3^{\circ}\text{C}$ and a mean annual precipitation of ~ 400 mm, while to the further northeast a desert-steppe landscape with modern mean annual temperature of $\sim 8^{\circ}\text{C}$, mean annual precipitation of ~ 110 mm, and mean annual possible evaporation up to ~ 2400 mm (Yu *et al.* 2006) exists.

Situated at the modern junction of the Asian Summer Monsoon and the Westerlies, the Minle section is dominated by the Westerlies in winter, and impacted by the Asian Summer Monsoon in summer

(An *et al.* 2012). Differently, the main body of the Chinese Loess Plateau located to the south of the modern Asian Summer Monsoon margin is impacted by the Asian Summer Monsoon in summer and the Asian Winter Monsoon in winter. The local Holocene moisture variation history based on the section has been reconstructed by optical, grain size, matrix carbonate content, total organic carbon and low-frequency magnetic susceptibility (χ_{LF}) analysis, suggestive of the longest and most intense humid period in the early Holocene and four sequences of long-term gradual wetting (several thousands of years) and subsequent abrupt drought (a few hundred years) on millennial to centennial timescales (Zhong *et al.* 2022).

3 MATERIAL AND METHODOLOGY

3.1 Material and sampling

The Minle section is 4.48 m thick and contains 11 PS layers and 8 PL layers (Fig. 2). Chronology of the Minle section has been constrained to 13.3–0.5 cal. ka BP by ^{14}C ages of 30 charcoal samples (Zhong *et al.* 2022). The section has a temporal resolution of in average ~ 35 cm ka^{-1} . PS1, PS3, PS5 and PS8–PS9 are more blackish. Generally, the PL layers have weaker pedogenesis processes than the PS layers based on total organic carbon and χ_{LF} . Among the PL layers, the pedogenesis degree of PL2–PL8 is higher than that of PL11. The eluviated calcium carbonate, a typical feature in loess deposits, is visible in the section.

After removing ~ 10 cm material on the outcrop surface of the Minle section, we sampled the fresh aeolian material at a 1-cm interval. Some samples were at a 0.5-cm interval. A total of 455 samples were obtained.

3.2 Methods and indices

In order to investigate the composition of magnetic minerals, we carried out integrated rock magnetic and DRS investigations (Table 1).

The χ - T curves were measured with a KLY-3 Kappa bridge using a CS-3 high-temperature furnace in an argon environment (flow rate of 100 ml min^{-1} , sensitivity of 1×10^{-8} SI, AGICO Ltd) from room temperature to 700 °C and then cooled back to room temperature. Contributions from the sample holder and thermocouple are subtracted. χ_{pre} and χ_{post} are the room temperature susceptibilities before and after a heating cycle, respectively. χ_{d} is the susceptibility loss caused by mineral inversion (such as inversion of maghemite to haematite) during heating (Liu *et al.* 2020). For the samples of PS8, χ_{d} is $\chi_{250-400^\circ\text{C}}$, which is the susceptibility difference between 250 and 400 °C on the heating curves. $\chi_{\text{post}} + \chi_{\text{d}}$ can be regarded as the total susceptibility when all Fe-bearing silicates/clays have been completely weathered to ferrimagnetic magnetite, and this parameter also can denote the total eolian input of weatherable Fe (Liu *et al.* 2020). Consequently, $\chi_{\text{pre}}/(\chi_{\text{post}} + \chi_{\text{d}})$ is able to represent the ratio of pedogenic iron to total weatherable Fe, and can be used as an effective weathering index (Gao *et al.* 2019; Liu *et al.* 2020).

The isothermal remanent magnetization (IRM) and hysteresis parameters of selected samples were measured using a vibrating sample magnetometer (MicroMag VSM 3900, Princeton Measurements Corporation). The applied field was cycled between ± 1.5 T for hysteresis loop measurement. Saturation magnetization (Ms), SIRM (Mrs) and coercivity (Bc) were determined after a high-field slope correction using a line fit through data points between 70 and 100 per cent of the maximum applied field. The IRM acquisition

curves were obtained in the fields from 0 to 1.5 T. After the saturation of Mrs, the samples were placed in a reverse magnetic field to get the remanence coercivity (Bcr) when the remanence is zero. The values of Mrs/Ms versus Bcr/Bc were then plotted on a Day diagram to show the domain state of the samples (Day *et al.* 1977; Dunlop 2002).

For each sample, 120 FORC were measured with an averaging time of 150 ms by the MicroMag VSM 3900. The FORC diagrams are simply given by the mixed second derivative (Roberts *et al.* 2000).

An ARM was imparted in an alternating field (AF) of 80 mT with a superimposed 50 μT bias field. This remanence is converted into anhysteretic susceptibility (χ_{ARM}). SIRM were measured in a steady constant field of 1 T and demagnetized at peak AF of 30, 60 and 100 mT. SIRM is not affected by paramagnetic and diamagnetic materials, reflecting only the contributions of ferrimagnetic minerals and antiferromagnetic minerals. All remanences were measured using a cryogenic magnetometer (Model 760, 2 G Enterprises) installed in a magnetically shielded room (< 300 nT). SIRM_{nmT} is used to represent the residual SIRM after an n mT AF demagnetization. The $\chi_{\text{LF}}/\text{SIRM}$ ratio is considered as the indicator for the concentration of small magnetic particles such as SP grains. The $\chi_{\text{ARM}}/\text{SIRM}$ ratio can be used as a grain size indicator for ferrimagnetic minerals, and it peaks in the SD range but decreases with increasing grain size (Maher 1988).

For DRS measurements, the samples were dried at a low temperature of 40 °C and then were ground in an agate mortar. The fine powdered samples were then pressed into orbicular plastic holders of 4 cm in diameter. Their absorption spectra were measured in the 200–2600 nm range using a Varian Cary 5000 UV–Vis–NIR spectrophotometer (Agilent Technologies Inc.) at 0.5 nm intervals with a scan rate of 300 nm min^{-1} . The DRS original data were transformed into Kubella–Munk function curves, which were analysed by using the first- and second-order derivative method (Torrent & Barron 2008). The haematite/(haematite + goethite) ratios determined by differential X-ray diffraction and by DRS show good linear correlation, so the DRS data can be used in the quantitative analysis of these two minerals (Torrent & Barron 2008). I_{Gt} and I_{Hm} are amplitudes of the bands between the minimum at ~ 415 nm and the maximum at ~ 445 nm and between the minimum at ~ 535 nm and the maximum at ~ 580 nm in the second-order derivative curves, respectively (Torrent & Barron 2008). The two indices represent the quantitative concentration of goethite and haematite.

At least one sample of each layer was measured for the χ - T curves, hysteresis parameters and FORC diagrams (Tables 1 and 2), and samples collected at every 1 cm were used for the ARM, SIRM and DRS measurements.

4 RESULTS

4.1 χ - T curves

In the heating curves, magnetic susceptibility increases clearly below 300 °C (Fig. 3a), which may be associated with the neoformation of fine-grained ferrimagnetic minerals from goethite or other Fe-hydroxides (Dunlop *et al.* 2004; Deng *et al.* 2005). All the samples display an inflection at 300 – 400 °C, suggesting that thermally unstable fine-grained maghemite (SP grains) starts to transform into weakly magnetic haematite (Maher 1998; Liu *et al.* 2005; Gao *et al.* 2019). The susceptibility drops between 300 and 400 °C can therefore be used to indicate the content of fine-grained maghemite

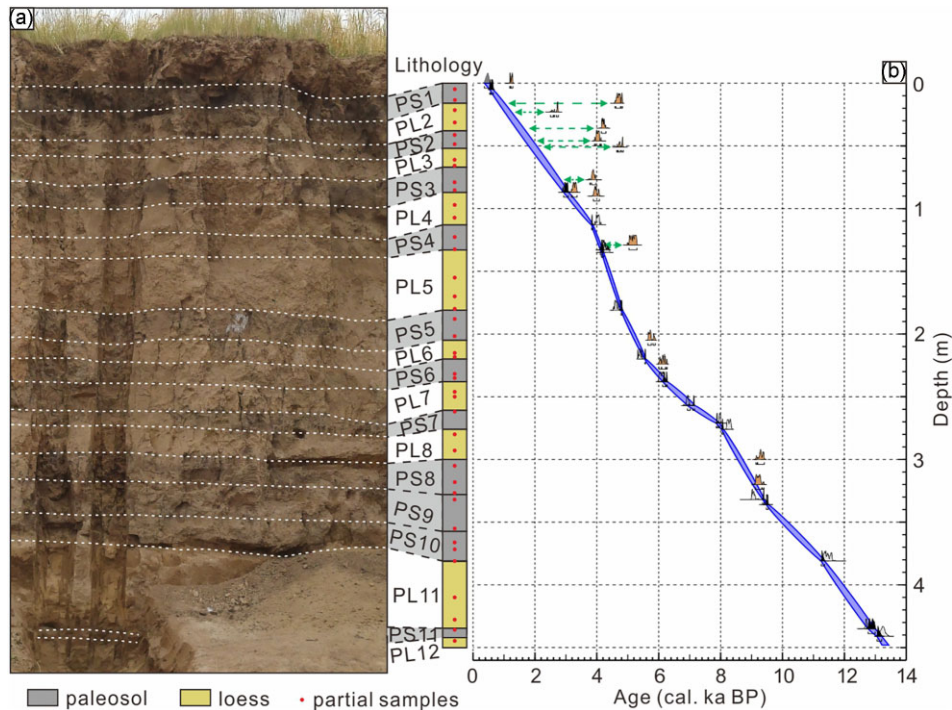


Figure 2. A field photo of the Minle section and the age–depth model based on youngest calibrated ^{14}C ages of charred materials (modified from Zhong *et al.* 2022). Red solid circles represent samples measured for the χ – T curves, hysteresis parameters and FORC diagrams (see Table 2 for more information). Please see the text for samples used for the ARM, SIRM and DRS measurements. PS, palaeosol layer and PL, loess layer.

Table 1. Definition of some magnetic parameters used in this paper.

Parameter	Definition	Notes
χ_{pre}	Room temperature susceptibility before a heating cycle	
χ_{post}	Room temperature susceptibility after a heating cycle	
χ_{d}	Susceptibility loss caused by mineral inversion (such as inversion of maghemite to haematite) during heating	The difference between the highest magnetic susceptibility near 250 °C and the lowest magnetic susceptibility near 400 °C during heating below ~400 °C
$\chi_{\text{pre}}/(\chi_{\text{post}} + \chi_{\text{d}})$	A weathering or pedogenic index	
SIRM	Saturation isothermal remanent magnetization	
I_{Gt}	Quantitative content of haematite	Amplitudes of the bands between the minimum at ~415 nm and the maximum at ~445 nm
I_{Hm}	Quantitative content of goethite	Amplitudes of the bands between the minimum at ~535 nm and the maximum ~580 nm
$I_{\text{Hm}}/I_{\text{Gt}}$	Ratio of the content of haematite to goethite	
$I_{\text{Hm}}/(I_{\text{Hm}} + I_{\text{Gt}})$	Ratio of the content of haematite to content sum of haematite and goethite	

(Liu *et al.* 2005; Liu *et al.* 2020; Yang *et al.* 2022), although the Curie temperature may play a role in the drops. Magnetic susceptibility drops sharply at 500–585 °C, indicating the Hopkinson effect and implying that magnetite is the dominant magnetic carrier (Dunlop *et al.* 2004). The PL12–PL11 samples show more obvious temperature-independent nature of low-field susceptibility below 585 °C than other samples (Fig. 3a).

The cooling curves have higher susceptibility than the heating curves, and most of them peak at 450 °C (Fig. 3b), which are indicative of the neof ormation of magnetite from iron-containing silicates/clays or the burning of organic matter (Fig. 3b, Liu *et al.* 2005; Lattard *et al.* 2006).

4.2 Hysteresis experiments

Most hysteresis loops are slightly wasp-waisted (Fig. 4), which have been interpreted as resulting from the competing contributions of the composition, concentration and grain size of magnetic minerals (Forster & Heller 1997; Deng *et al.* 2005). The loops do not close even at 500 mT, especially for PL12–PL11. On the contrary, the PS8 sample shows a thinner hysteresis loop than all the other layers (Fig. 4).

In addition, the Day diagram indicates that the magnetic mineralogy of the samples from PS10–PS1 are dominated by pseudo-single-domain (PSD) grains (Fig. 5, Day *et al.* 1977; Dunlop 2002). PSD behaviour is due to pure PSD grains and/or superimposed

Table 2. Partial test items of the Minle section.

Layer	Depth (m)	Age (a BP)	Age error (a)	$\chi-T$	Hysteresis loop	Isothermal remanent magnetization (IRM)	First-order reversal curve (FORC)
PS1	0.06	631.20	34.3	✓	✓	✓	✓
	0.13	837.20	46		✓	✓	
PL2	0.21	1072.60	54.7	✓	✓	✓	✓
	0.31	1366.80	61.4		✓	✓	
PS2	0.41	1661.00	64.8	✓	✓	✓	✓
	0.49	1896.40	65.5		✓	✓	
PL3	0.61	2249.70	63.1		✓	✓	
	0.66	2396.90	60.9	✓	✓	✓	✓
PS3	0.79	2779.40	51.2		✓	✓	
	0.85	2955.90	43.7	✓	✓	✓	✓
PL4	0.97	3335.40	43.7		✓	✓	
	1.07	3656.10	33.1	✓	✓	✓	✓
PS4	1.23	4003.70	18.4		✓	✓	✓
	1.33	4158.80	15.9	✓	✓	✓	✓
PL5	1.55	4454.60	22.6		✓	✓	✓
	1.70	4655.90	19.5		✓	✓	
	1.80	4790.10	11.5	✓	✓	✓	✓
PS5	1.88	4940.40	22.6	✓	✓	✓	✓
	2.035	5243.600	27.5		✓	✓	
PL6	2.15	5468.60	18.9		✓	✓	
	2.19	5546.80	10	✓	✓	✓	✓
PS6	2.32	5992.00	43.2		✓	✓	
	2.36	6133.80	44.4	✓	✓	✓	✓
PL7	2.46	6577.20	64.9		✓	✓	
	2.50	6763.20	70.3	✓	✓	✓	✓
PS7	2.62	7376.30	68.2		✓	✓	
PL8	2.80	8160.60	27.6	✓	✓	✓	✓
	2.93	8467.10	39	✓	✓	✓	✓
PS8	3.05	8750.00	41		✓	✓	
	3.18	9056.50	35.6	✓	✓	✓	✓
	3.27	9268.80	24.9	✓	✓	✓	✓
PS9	3.32	9386.70	11.4	✓	✓	✓	✓
	3.54	10 226.00	60.2		✓	✓	
PS10	3.67	10 742.90	58.7	✓	✓	✓	✓
	3.71	10 901.90	54.3		✓	✓	
	3.81	11 299.50	28.5	✓	✓	✓	✓
PL11	4.10	12 147.30	62.9	✓	✓	✓	✓
	4.28	12 673.50	67.5		✓	✓	
PS11	4.36	12 917.90	62.8	✓	✓	✓	✓
PL12	4.44	13 201.70	46.4	✓	✓	✓	✓

independent SD and MD moments (Dunlop 2002). The samples from PL12–PL11 are closer to the Bcr/Bc-axis and farther from the Mrs/Ms-axis than other samples, but the samples from PS8 are located at the other end of the distribution area.

4.3 FORC diagrams

The FORC diagrams of samples above PL11 show a separate peak centered at B_c of ~ 10 mT and secondary peak constrained by small '>' shaped contours at the origin (Figs 6a–g). The PS7–PS1 samples have a weaker part of the FORC distribution than the PS10–PS8 samples. They all show three-lobe configuration of outer contours, but the PS7–PS1 samples have a weaker part of the FORC distribution than the PS10–PS8 samples. The upward shift of the FORC distribution is only remarkable in the absence of magnetic interactions. The secondary peak constrained by small '>' shaped contours adjoining the origin of the FORC diagram indicate that the

distribution has been shifted to lower coercivities by thermal relaxation effects. Vertical contours in the left-hand portion of the FORC diagrams that lie nearly parallel to the B_i axis are also produced as a result of thermal relaxation in calculations.

The FORC diagrams from PL12–PL11 (Figs 5h–j) show near-vertical open contours at the origin.

4.4 Weathering index

The variations of the $\chi_{pre}/(\chi_{post} + \chi_d)$ ratios, positively correlated with the weathering index (Liu *et al.* 2020), show the lowest values of 0.05–0.12 in PL12–PL11 and highest ratios of ~ 0.20 –0.30 in PS10–PS8 (Fig. 7a). The ratios rapidly decline from PS8 to PL8, and then are mostly steady between 0.11–0.14 in PS7–PL6. A slight increase is observed for the layers above PL6, with ratios between 0.15–0.20. Additionally, more variations are observed from PS3 to PL3.

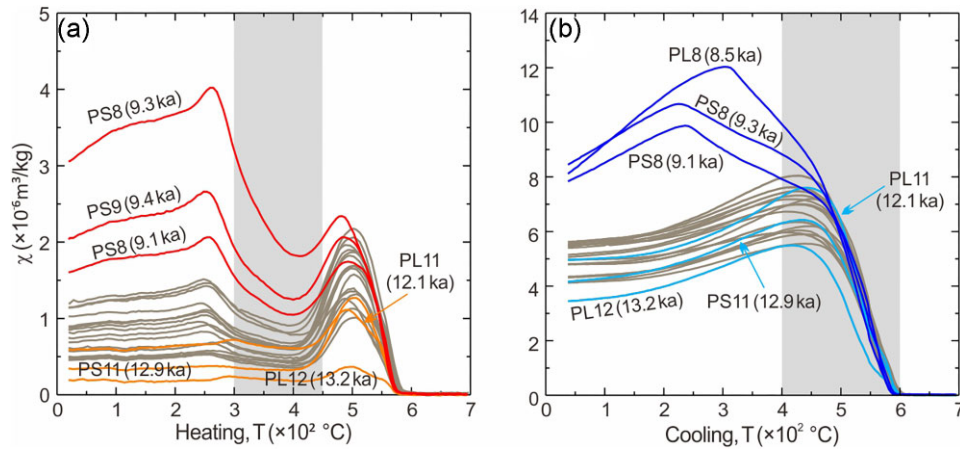


Figure 3. (a) Warming and (b) cooling runs of χ for the 23 selected samples. Grey bars highlight a gradual decrease of susceptibility between 300 and 400 °C during warming and a gradual increase between 600–400 °C during cooling, respectively. In (a), red curves show samples taken from layer PS8, and samples from PL12–PL11 are shown in orange. Their ages are shown in bracket. In (b), samples from PS8 and PL8 are shown in dark blue, and samples from PL12–PL11 is shown in light blue.

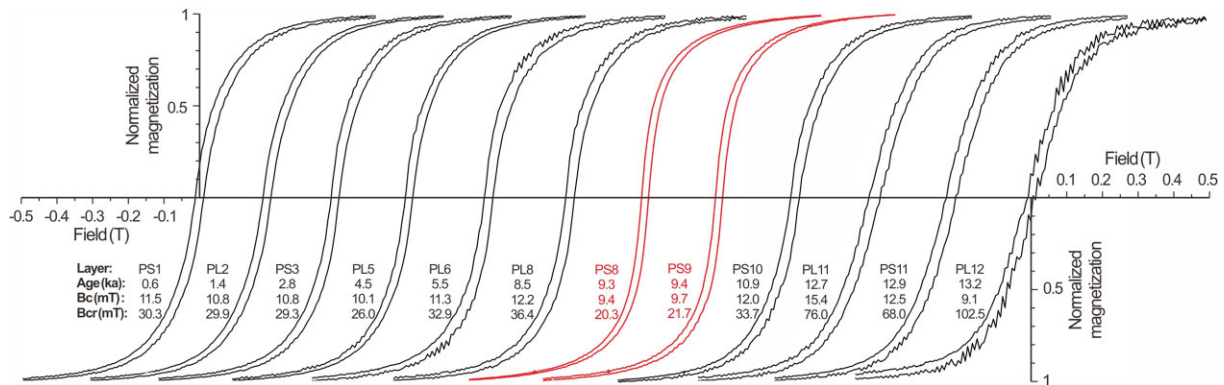


Figure 4. Hysteresis loops for representative PS and PL samples after slope correction for paramagnetic contribution.

4.5 ARM and SIRM curves

The curves of χ_{ARM} and SIRM yield almost identical linear relationships as that of χ_{LF} (Figs 7b–d, Zhong *et al.* 2022). Generally, PS layers have higher values than PL layers. Two strong peaks in PS10–PS8 are the most prominent features of the section. The χ_{ARM} , SIRM and χ_{LF} are higher in PS5–PS1 than in PS7–PL6. In addition, the peaks in PS3 and PS2 are also distinguishable. The SIRM in the PS layers, especially in PS10–PS8, is more easily AF demagnetized than that in the loess layers (Fig. 7d, Deng *et al.* 2006). PS SIRM shows the sharpest decrease in intensity between 0 and 30 mT in all PS and PL layers. In particular, SIRM_{nmT} and $\text{SIRM}_{30-100\text{mT}}/\text{SIRM}$ ratios show an upward increase in fluctuations with increasing AFs (Figs 7d and e).

The $\chi_{\text{LF}}/\text{SIRM}$ ratios are the lowest in PL12–PL11 and the highest in PS9–PS8 (Fig. 7f). Similarly, the $\chi_{\text{ARM}}/\text{SIRM}$ ratios are the lowest in PL12–PL11 and the highest in PS10–PS8 with average ratios of 1.15 and 4.28 (Fig. 7g). The average $\chi_{\text{ARM}}/\text{SIRM}$ ratio of the samples from the layers above PL8 is 3.52.

4.6 DRS results

All the samples show remarkable peaks at 558 and 435 nm in the first-order derivative curves (Fig. S1, Supporting Information), which has been suggested as an indicator for the existence of

haematite and goethite in both PL and PS layers (Deaton & Balsam 1991). I_{Hm} and I_{Gt} calculated from the second-order derivative curves (Fig. S2, Supporting Information) show different change modes (Figs 7h and i). I_{Hm} curve shows the lowest values in PL12–PL11 and the highest ones in PS8, but no clear changes in the other layers. I_{Gt} curves show the highest values in PL11, and the lowest values in PS8–PS10 and PS11. I_{Gt} values of PS7–PS3 are higher than those of PL3–PS1. Interestingly, $I_{\text{Hm}}/I_{\text{Gt}}$ and $I_{\text{Hm}}/(I_{\text{Hm}} + I_{\text{Gt}})$ curves show one peak in PS8 and PS10 like SIRM curves, but no obvious changes in the other layers (Figs 7j and k).

5 DISCUSSION

5.1 Magnetic minerals and grain size

The measurements and analyses indicate the existence of maghemite, magnetite, haematite and goethite in the Minle section.

Samples from PS8 show the maximum declines during heating from 300–400 and 500–585 °C in the χ – T heating curves (Fig. 3) and the highest magnetic susceptibility (Fig. 7), which implies the high content of fine-grained maghemite and magnetite. On the contrary, limited variations of magnetic susceptibility with temperature suggest that PL12–PL11 samples have low content of the two minerals but high content of partially oxidized aeolian coarse-grained MD-like magnetite (Figs 3 and 7, Liu *et al.* 2020). The

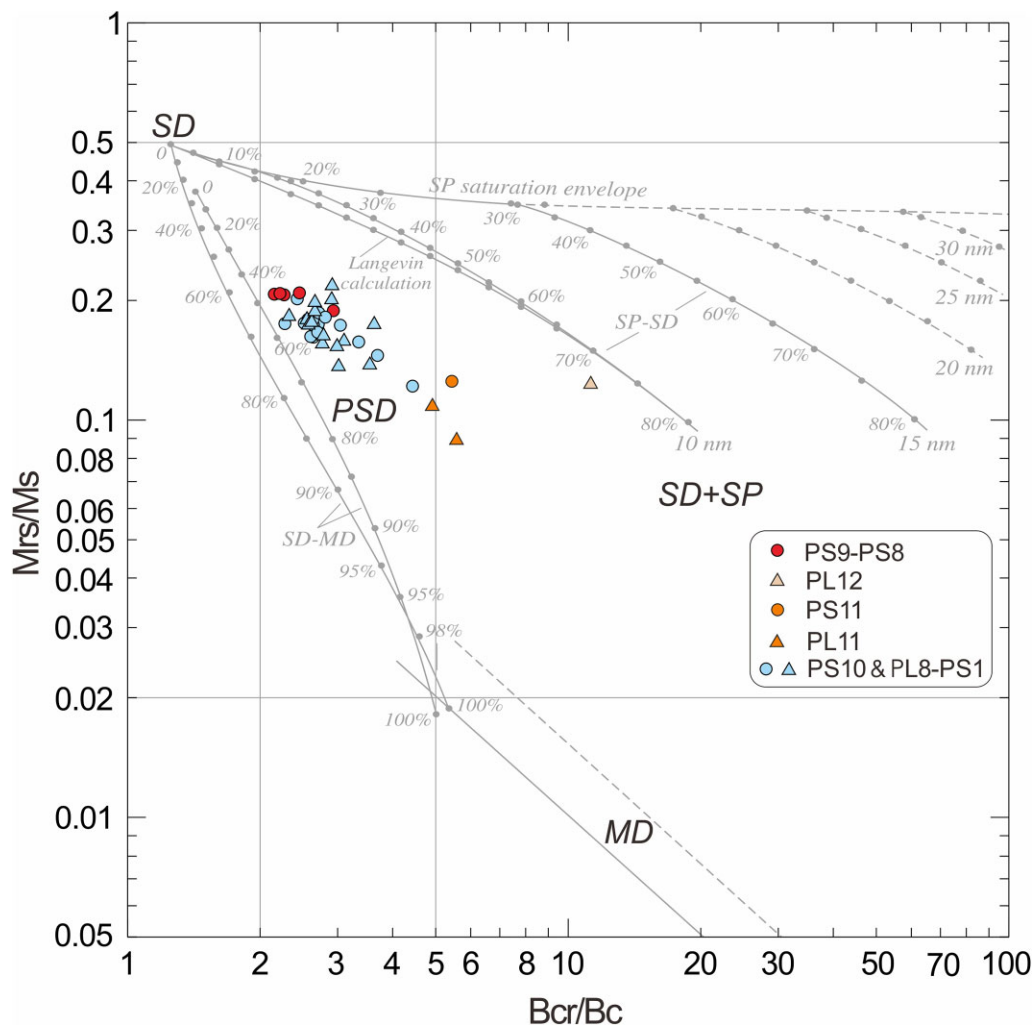


Figure 5. Hysteresis ratios plotted on a Day diagram (Day *et al.* 1977) of the PS (circles) and PL (triangles) samples of the Minle section. The curves are theoretical Day plot curves calculated for magnetite, and the numbers along curves are volume fractions of the soft component (SP or MD) in mixtures with SD grains (Dunlop 2002). Orange circles and triangles are the samples from PL12–PL11 layers. SD: single domain; PSD: pseudo-single domain; MD: multidomain; SP: superparamagnetic; Mrs: saturation isothermal remanent magnetization; Ms: saturation magnetization; Bcr: coercivity of remanence and Bc: coercivity.

phenomena are supported by the thinnest hysteresis loops of PS8 samples and the widest ones of PL12–PL11 samples (Fig. 4). In addition, the open nature of hysteresis loops above 500 mT indicates that high-coercivity phases are present in all layers except in PS8 (Fig. 4), while PL12–PL11 have a higher component of high-coercivity phases than the other layers (Fig. 5). The two-end distribution of the two types of samples on the Day diagram also indicates that there are larger PSD and MD-like magnetic grains in PL12–PL11 but more SD component in PS8 (Fig. 5, Liu *et al.* 2004; Deng *et al.* 2005). The separate peak, secondary peak and three-lobe configuration of the FORC diagrams of samples above PL11 indicate the existence of a non-interacting SD component, particles that have lost their coercivity (i.e. very fine-grained SP grains) and a PSD component (Roberts *et al.* 2000; Smirnov 2006; Li *et al.* 2022b; Yang *et al.* 2022). The near-vertical open contours at the origin of the FORC diagrams from PL12–PL11 suggest the presence of an MD component with a high proportion of high-coercivity minerals such as haematite, goethite and partially oxidized aeolian coarse-grained magnetite (Figs 6h–j, Roberts *et al.* 2006; Li *et al.* 2022b).

Importantly, all the $\chi_{\text{pre}}/(\chi_{\text{post}} + \chi_{\text{d}})$, χ_{LF} , χ_{ARM} , SIRM_{nmT} , $\chi_{\text{LF}}/\text{SIRM}$ and $\chi_{\text{ARM}}/\text{SIRM}$ ratios are the lowest in PL12–PL11 and highest in PS10–PS8 (Figs 7a–g), implying the lowest and highest content of SP and SD components in PL12–PL11 and PS10–PS8, respectively, which suggest that PL12–PL11 contain more MD component than the other layers.

DRS results indicate different variation modes of the concentration of haematite and goethite. The content of haematite is highest in PS8 and lowest in PL12–PL11. The content of goethite is highest in PL11 and lowest in PS10–PS8 (Figs 7h–k).

5.2 Magnetic enhancement and pedogenesis

The ferrimagnetic assemblage in the Chinese loess consists of a mixture of aeolian coarse-grained magnetite and low-Ti titanomagnetite (Maher & Thompson 1992), and pedogenic fine-grained ferrimagnetic minerals (Zhou *et al.* 1990; Hu *et al.* 2015; Gao *et al.* 2019). The fine-grained grains are mainly SP and SD components, and the corresponding mineral is maghemite rather than magnetite, because these pedogenic ferrimagnetic particles with high surface

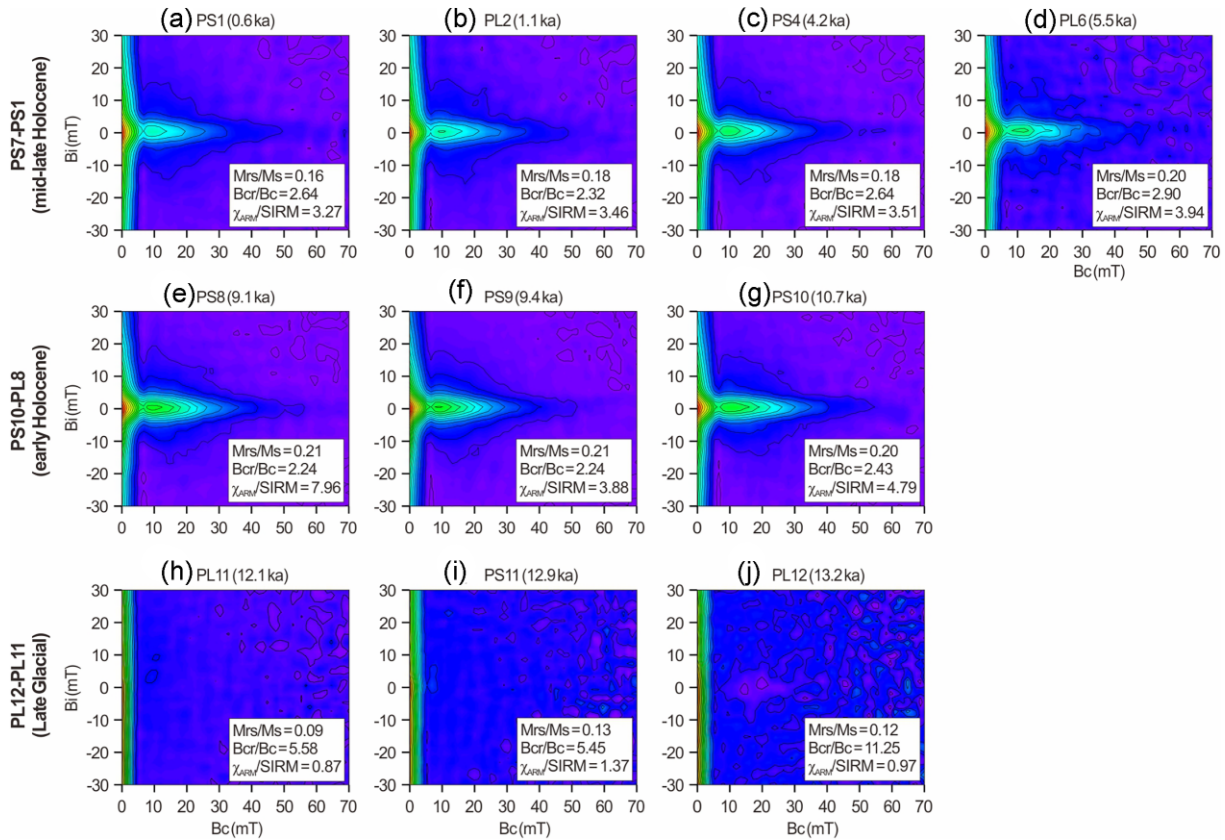


Figure 6. FORC diagrams of representative samples. The vertical axis (B_i) shows the degree of magnetostatic interactions between grains. The horizontal axis (B_c) displays the coercivity distribution of the different magnetic grain size and mineralogy components within the sample. Smoothing factor is 4 for all samples. The units for values of $\chi_{\text{ARM}}/\text{SIRM}$ are 10^{-4} m A^{-1} .

to volume ratios are eventually oxidized into maghemite regardless of their initial states (magnetite or maghemite, Mullins 1977; Maher 1998; Liu *et al.* 2007). Pedogenesis can further oxidize the coarse-grained lithogenic magnetite, thus decreasing the coercivity of magnetite (Liu *et al.* 2004). The magnetic enhancement in PSs is mainly determined by the concentration of pedogenic particles, rather than their grain size. SD grains contribute more than half of the enhanced magnetic susceptibility in PSs (Liu *et al.* 2004).

Lower $\chi_{\text{pre}}/(\chi_{\text{post}} + \chi_d)$, χ_{LF} , χ_{ARM} , SIRM_{nmT} , $\chi_{\text{LF}}/\text{SIRM}$ and $\chi_{\text{ARM}}/\text{SIRM}$ in PL layers than PS layers (Figs 7a–g), and clear linear relationships between χ_{LF} , SIRM , $\chi_{\text{LF}}/\text{SIRM}$, $\chi_{\text{ARM}}/\text{SIRM}$ and χ_{ARM} (Fig. 8) suggest that the magnetic enhancement was mainly caused by magnetite and maghemite of SP and SD components produced by *in situ* pedogenesis. However, SP component also contributes to susceptibility increase in PS9–PS8 due to the significant peaks of $\chi_{\text{LF}}/\text{SIRM}$ curve (Fig. 7f). With an increasing degree of pedogenesis, the concentration of SP and SD particles increases, and thus the overall grain size of the PL–PS sequences becomes finer.

PL layers exhibit higher coercivities as supported by higher $\text{SIRM}_{30-100\text{mT}}/\text{SIRM}$ ratios (Fig. 7e). Four magnetic components may contribute to $\text{SIRM}_{0\text{mT}}$: pedogenic maghemite/magnetite, partially oxidized aeolian coarse-grained magnetite, aeolian haematite and goethite, and pedogenic haematite and goethite (Deng *et al.* 2006). The 30 mT AF demagnetization remarkably weakens the contributions of pedogenic ferrimagnetic particles to SIRM (Figs 7d and e). Partially oxidized aeolian coarse-grained magnetite and haematite/goethite significantly contribute to the intensity of

$\text{SIRM}_{60\text{mT}}$ (Figs 7d and e, Deng *et al.* 2006). In addition, 100 mT AF demagnetization can partly remove the contributions of these particles and enhance the relative contributions of magnetically harder phases simultaneously (Figs 7d and e, Deng *et al.* 2006; Liu *et al.* 2007). Considering the uniform values of haematite concentration in the whole section, the lowest goethite concentration in PS10–PS8 (Figs 7h and i) and negligible contribution of haematite and goethite to magnetic susceptibility, we propose that $\text{SIRM}_{100\text{mT}}$ is controlled by the partially oxidized aeolian coarse-grained magnetite. Thus $\text{SIRM}_{100\text{mT}}/\text{SIRM}$ ratio can be used as a proxy for variations in the relative contributions of partially oxidized aeolian coarse-grained magnetite.

5.3 Interpretation of the long-term mineral magnetic variations

Based on the variations of $\chi_{\text{pre}}/(\chi_{\text{post}} + \chi_d)$, χ_{LF} , χ_{ARM} , SIRM and the moisture index (Figs 7a–d and 9a), the Minle section can be divided into four substages: PL12–PL11 (13.3–11.7 ka), PS10–PL8 (11.7–8.1 ka), PS7–PL6 (8.1–5.3 ka) and PS5–PS1 (5.3–0.5 ka), respectively, corresponding to the Late Glacial, early Holocene, middle Holocene and late Holocene.

Concentration of different magnetic minerals may reveal the chemical weathering intensity of source areas in glacial stages and of sedimentary areas during interglacial stages (Deng *et al.* 2006). Fe input is rarely considered as a limiting factor for the formation of magnetic susceptibility in loess (Maher 1998; Hu *et al.* 2015).

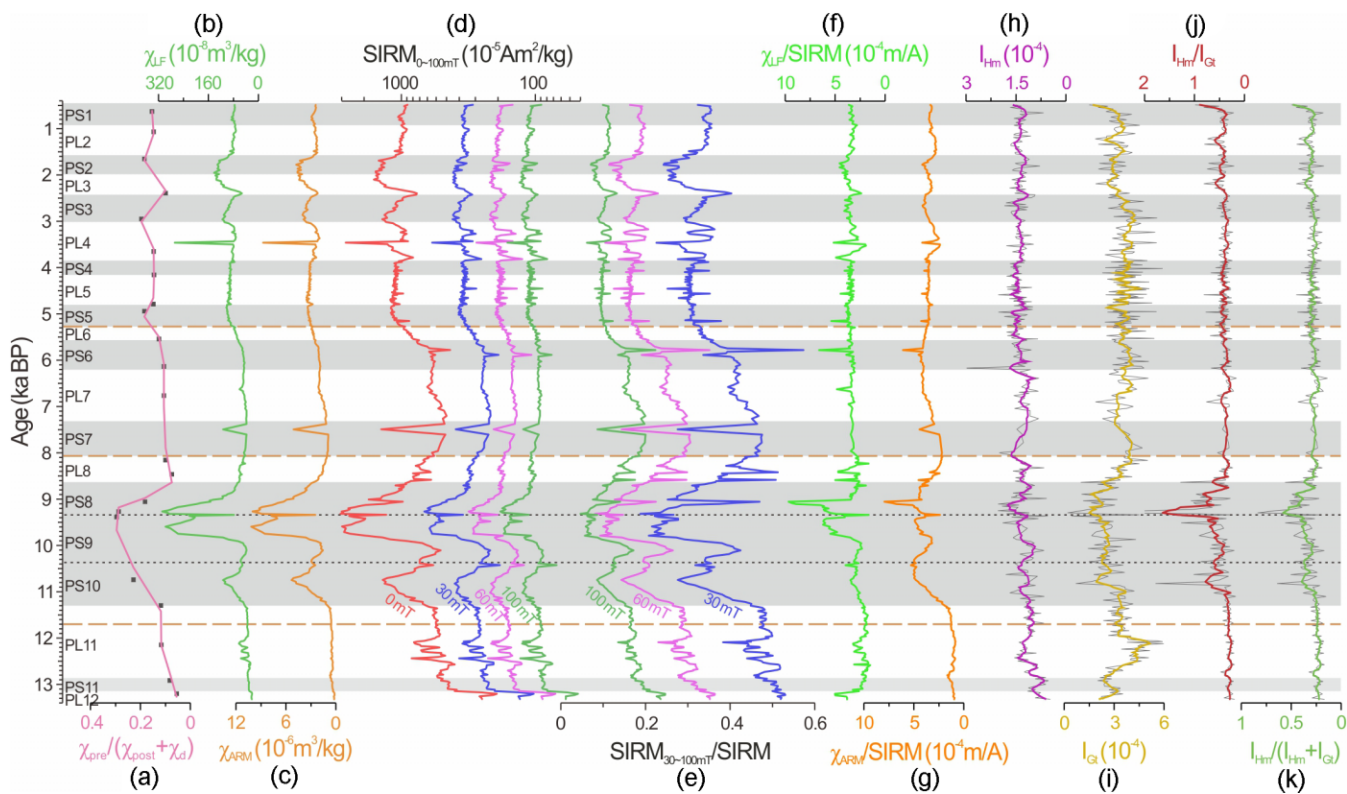


Figure 7. Magnetic parameter changes of the Minle section. (a) Weathering index indicated by $\chi_{pre}/(\chi_{post} + \chi_d)$ ratios. (b) χ_{LF} (Zhong *et al.* 2022). (c) χ_{ARM} . (d) Intensity of the initial SIRM and SIRM after AF demagnetization at peak fields of 30, 60 and 100 mT on a logarithmic axis. (e) Stratigraphic variations of the residual SIRM after AF demagnetization normalized by the initial SIRM. The variations are dimensionless. (f) and (g) $\chi_{LF}/SIRM$ and $\chi_{ARM}/SIRM$ as indices of content of SP and SD components, respectively. (h) and (i) I_{Hm} and I_{Gt} characterize haematite and goethite concentration. (j) and (k) I_{Hm}/I_{Gt} and $I_{Hm}/(I_{Hm} + I_{Gt})$ characterize the content of haematite relative to content of goethite and to sum content of haematite and goethite based on DRS.

The Minle section is located at the northern margin of the Qilian Shan, and the deserts in the north are its potential source areas (Fig. 1). Dry climates of the deserts are not conducive to pedogenesis and formation of pedogenic fine-grained maghemite/magnetite and goethite (Deng *et al.* 2006; Hu *et al.* 2015). Limited variations in haematite content suggest few changes of Fe input (Fig. 9g). Additionally, Zircon U–Pb ages and heavy mineral assemblage indicate that there is no significant change in the provenance for the Minle section loess between the Late Glacial and Holocene (unpublished data). During pedogenic processes, haematite or other iron oxides can be reduced to magnetite under wet conditions with organic matter and iron-reducing bacteria, and then be oxidized into maghemite in subsequent dry periods (Maher 1998; Barrón & Torrent 2002). However, the transitions might be too weak to influence the total concentration. Consequently, dust origin should have had little impact on magnetic minerals of the Minle section since the Late Glacial.

PS11 and PL11 layers were deposited during the Late Glacial, which was the driest and coldest period in the past 13.3 ka, especially for PL11 deposited in the Younger Dryas (Fig. 9a, Zhong *et al.* 2022). This cold and dry climate could only maintain plant communities with low productivity. The lowest $\chi_{pre}/(\chi_{post} + \chi_d)$, χ_{LF} , χ_{ARM} , SIRM and I_{Hm} of PL12–PL11 (Figs 7a–h) indicate that chemical weathering and pedogenesis during the Late Glacial were the weakest, producing the lowest concentration of pedogenic maghemite/magnetite

and partially oxidized aeolian coarse-grained magnetite. However, the two layers show the highest goethite concentration, which is similar to the Ganzi loess section in the eastern Tibetan Plateau (Hu *et al.* 2015). These observations indicate that goethite formation is favoured by cold climates.

During the early Holocene, PS10–PS8 layers showed rapid decrease of SIRM intensity, especially between 0 and 30 mT (Fig. 7d), suggesting that the concentration of pedogenic maghemite/magnetite reached the highest in them. Most of the other indices also support the strongest pedogenesis (Fig. 7). The period is suggested as the longest and strongest humid stage in response to a combination of the strongest Asian Summer Monsoon and the weakest, more poleward Westerlies, modulated by the highest summer insolation during the Holocene (Zhong *et al.* 2022). In addition, meltwater from glaciers, permafrost and snow may offset the highest potential evapotranspiration, which could also enhance local hydrological cycles (Rao *et al.* 2019). The early Holocene as a climatic optimum during the Holocene was triggered by the wettest climate (Fig. 9a) and possibly the highest temperature related to the strongest solar radiation (Fig. 9b). The concentration of magnetic minerals related to pedogenesis increased rapidly. It is noteworthy that the Minle section shows higher χ_{LF} values in PS9–PS8 than the Holocene loess sections on the Chinese Loess Plateau, Tibetan Plateau and central Asia (Fig. 10). The factors mentioned above might collectively create the ‘super pedogenesis’ and associated high magnetic susceptibility in the Minle section. The lowest

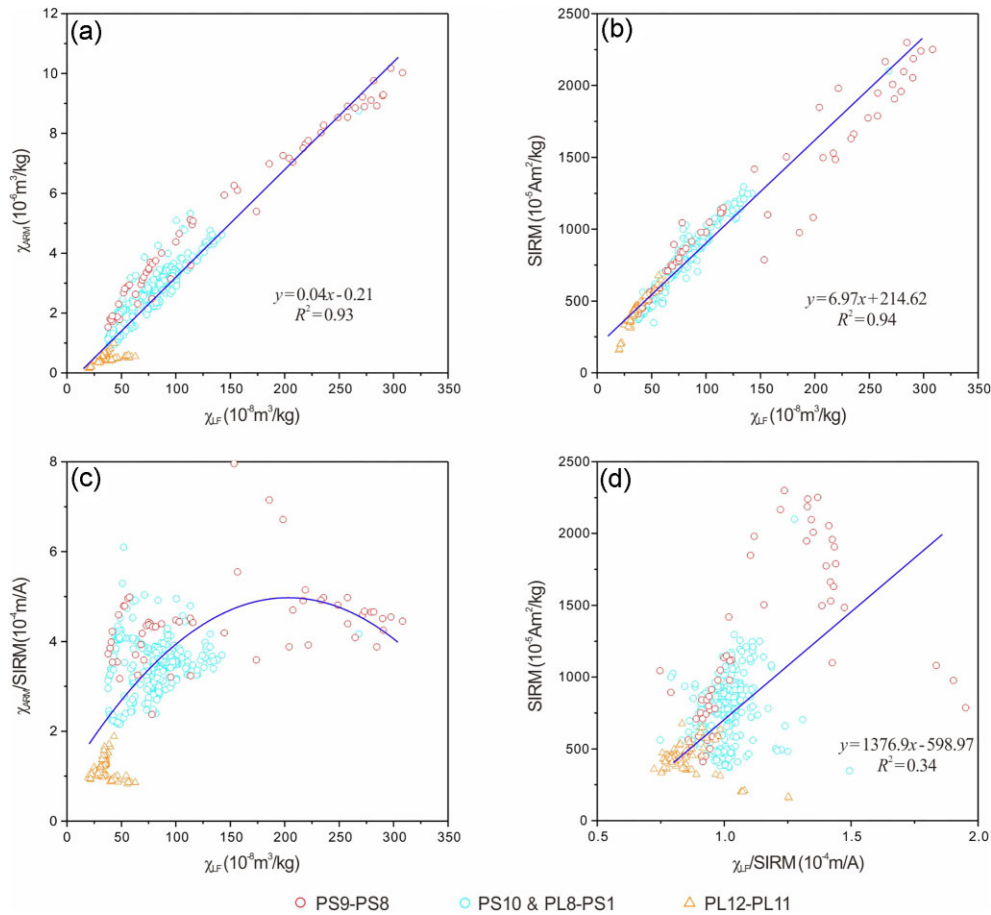


Figure 8. Relationship between (a) χ_{LF} versus χ_{ARM} ; (b) χ_{LF} versus SIRM; (c) χ_{LF} versus $\chi_{ARM}/SIRM$ and (d) $\chi_{LF}/SIRM$ versus SIRM for the Minle section.

goethite concentration in PS10–PS8 indicates that it hardly forms under high temperature (Figs 9b and h).

In PS7–PL6, little change of SP component characterized by $\chi_{LF}/SIRM$ indicates that the SD component characterized by $\chi_{ARM}/SIRM$ and partially oxidized aeolian coarse-grained magnetite characterized by $SIRM_{100mT}$ are important contributors to susceptibility, as they show in pace trends (Figs 9e and f). Moreover, lower values of many indices in PS7–PL6 than in PS5–PS1 (Fig. 9) suggest that pedogenesis was the weakest in PS7–PL6 within the Holocene. The solar insolation gradually decreased from ~ 10 ka to present (Fig. 9b). During the middle Holocene, as the solar insolation decreased, the Westerlies intensified and migrated equatorwards. Besides, the Asian Summer Monsoon weakened (Jiang *et al.* 2020; Yan *et al.* 2020), which collectively made it hard for the convective monsoon precipitation to reach the Asian Monsoon marginal zone (Zhang *et al.* 2021b; Zhong *et al.* 2022). In addition, higher temperatures related to the still high solar radiation caused high potential evapotranspiration (Orgeira *et al.* 2011; Hu *et al.* 2015), which could not maintain high productive plant communities. In fact, central Asia was generally dry during this period (Herzschuh 2006).

A possible explanation for the lower-amplitude fluctuations of the magnetic indices during the late Holocene (Figs 7a–d) could be that lower evapotranspiration resulted in increased effective humidity (Trouet *et al.* 2009; Chen *et al.* 2010), which led to denser vegetation, and in turn increased rainfall through regional hydrological cycles and biophysical processes (Ganopolski *et al.* 1998; Zhao & Yu

2012). Increased moisture transport by enhanced winter Westerlies might be another factor (Chen *et al.* 2016; Gao *et al.* 2022). This could explain the similar moisture index peaks but very different magnetic indicators between PS5–PS1 and PS10–PS8 (Fig. 9a).

5.4 Spatiotemporal differences in climate change recorded by loess in china

Comparing the χ_{LF} records of the loess sections in China, we find that the Holocene optimum corresponding to the strongest pedogenesis is different in time and space (Figs 1 and 10). The climatic optimum is in the early Holocene on the Tibetan Plateau and near the modern Asian Summer Monsoon margin but in the middle Holocene in the core area of the Chinese Loess Plateau, while central Asia shows a wetting trend during the Holocene. We suggest that the precipitation and effective humidity (a function of precipitation, evaporation and temperature) controlled by different climate systems are the key factors (An *et al.* 2000; He *et al.* 2004; Zhong *et al.* 2022).

In central Asia, winter insolation experienced an increasing trend during the Holocene (Figs 1 and 9b, Berger & Loutre 1991; Laskar *et al.* 2004), which could have caused enhanced evaporation over the mid-latitude region. Both the enhanced evaporation and westerly winds would have increased the moisture transport to the core area of central Asia, contributing to the observed Holocene wetting trend (Chen *et al.* 2010; Ran & Feng 2013; Chen *et al.* 2016). This phenomenon has been observed in multiple loess sections in Xinjiang,

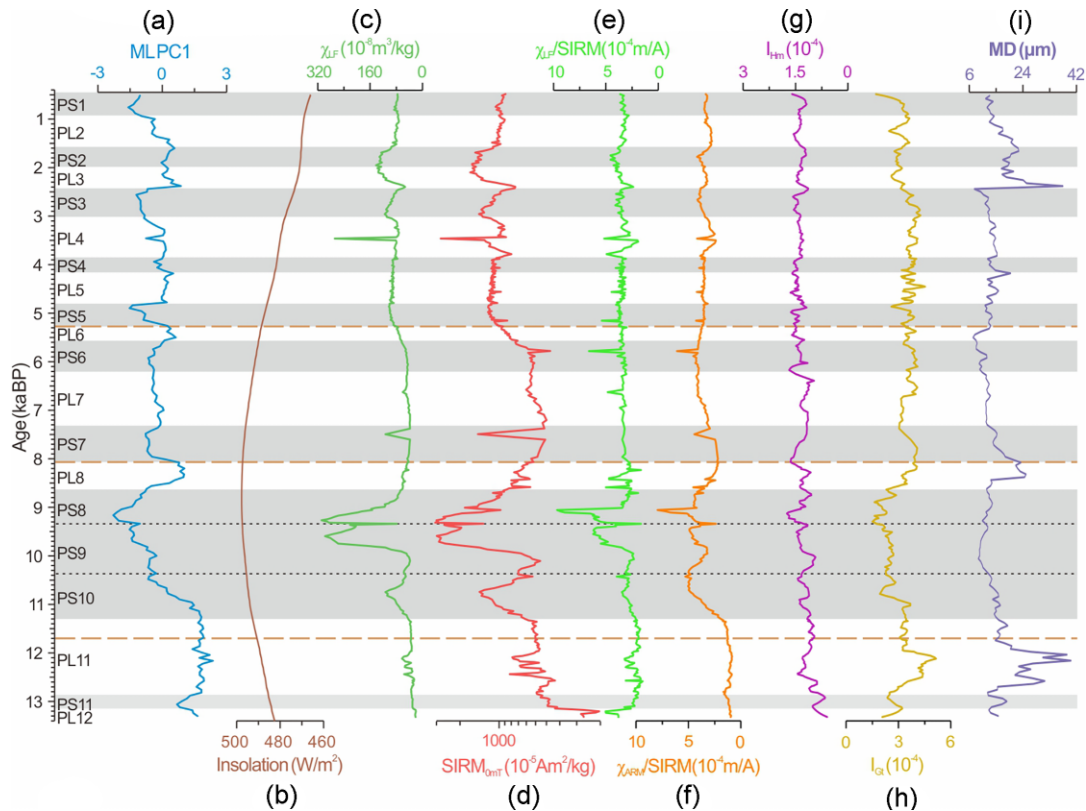


Figure 9. Comparison between magnetic parameters and hydroclimate records. (a) Moisture index ML PC1 (Zhong *et al.* 2022). (b) Insolation on a centennial scale at 37° N on July 23 was generated using La2004 solution (solar constant is 1365 w m^{-2} , Laskar *et al.* 2004; Li *et al.* 2019). (c) χ_{LF} (Zhong *et al.* 2022). (d) Intensity of the initial SIRM. (e) χ_{LF}/SIRM indicating content of SP component. (f) χ_{ARM}/SIRM indicating content of SD component. (g) I_{Hm} showing haematite concentration. (h) I_{Gt} showing goethite concentration. (i) Medium grain size (MD) of the Minle section (Zhong *et al.* 2022).

central Asia, such as the Lujiaowan section (Fig. 10j, Chen *et al.* 2016). A similar wetting trend since the middle Holocene suggested by the Minle section (Fig. 10a) support the influence of the West-erlies (Ran & Feng 2013), although increased effective humidity caused by local hydrological cycles cannot be ignored.

In the Asian monsoon region, monsoon precipitation and effective moisture are the most important factors controlling biological productivity, especially in arid, semi-arid and semi-humid areas that are sensitive to variations of the monsoon climate (Fig. 1, An *et al.* 2000; He *et al.* 2004). Although the solar radiation began to increase before 15 ka (Fig. 9b), the remnant ice sheets and the lowered concentration of carbon dioxide in the atmosphere during the last glaciation delayed the development and the advance of the East Asian Summer Monsoon (An *et al.* 2000; Zhang *et al.* 2021a). At 11–9 ka, summer (July) solar radiation in the Northern Hemisphere reached a maximum (Fig. 9b, Berger & Loutre 1991; Laskar *et al.* 2004), which triggered the northernmost frontal zone of monsoon rainfall to advance northward into the north of the modern Asian Summer Monsoon margin, causing a peak in precipitation that was reached early in the Holocene (An *et al.* 2000; He *et al.* 2004). As solar radiation weakened, a corresponding weakening of the summer monsoon caused the northernmost frontal zone to retreat (Fig. 9b, An *et al.* 2000). The Minle and Hepingzhen loess sections (Figs 1 and 10, Liang *et al.* 2021), and the lacustrine records near the modern Asian Summer Monsoon margin (Herzschuh *et al.* 2004; Chen *et al.* 2006; Zhong *et al.* 2022, and references therein) all indicate the highest χ_{LF} and moisture index during the early Holocene. While the highest χ_{LF} and moisture index of the middle Holocene

in sections on the Chinese Loess Plateau (Kang *et al.* 2011; Lu *et al.* 2013; Dong *et al.* 2015; Hu *et al.* 2015; Li *et al.* 2022a) could account for the summer monsoon retreat (Figs 1 and 10).

The climate of the Tibetan Plateau developed toward wetter and warmer conditions at ca. 10 ka. The ablation of ice and snow caused by rising postglacial temperature perhaps further strengthened the Tibetan Plateau Monsoon (An *et al.* 2000; Dong *et al.* 2015). The seasonal contrast between the thermodynamics of the plateau and that of the surrounding areas is the main driving force for the Plateau monsoon (Fig. 1, Tang *et al.* 1979). The Tibetan Plateau is much more sensitive, and responds more quickly to climatic changes than does eastern China (An *et al.* 2000; He *et al.* 2004). The unique climate system led to the wettest early Holocene on the Tibetan Plateau (Ran & Feng 2013), recorded by multiple and different sedimentary records, such as the Minle, Hepingzhen and Ganzi loess sections (Hu *et al.* 2015; Liang *et al.* 2021; Zhong *et al.* 2022, and references therein).

However, we should note that the climatic events suggested by different sections in the same climate model were asynchronous within China (Fig. 10). For example, the Minle, Hepingzhen and Ganzi sections show a dislocation of > 1 ka of the optimum during the early Holocene (Hu *et al.* 2015; Liang *et al.* 2021). As another example, the sections on the Chinese Loess Plateau show very different variation models, although they all show the optimum in the middle Holocene (Fig. 10, Kang *et al.* 2011; Lu *et al.* 2013; Dong *et al.* 2015; Hu *et al.* 2015; Li *et al.* 2022a). Besides precipitation and effective humidity under different climate systems, aeolian deposition processes may be one of the most important control factors

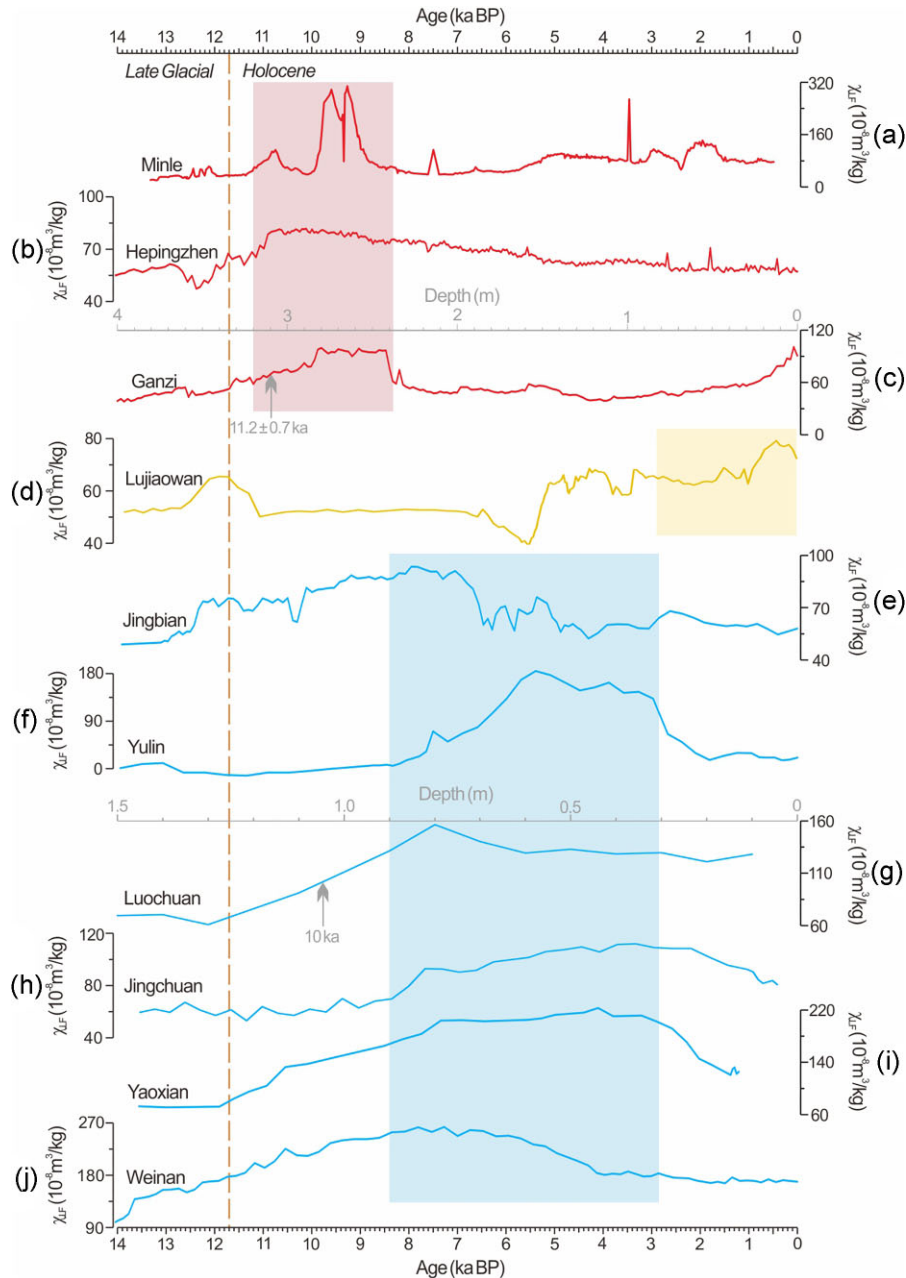


Figure 10. Comparison between low-frequency magnetic susceptibility (χ_{LF}) of the loess sections in China. (a) Minle, (b) Hepingzhen (Liang *et al.* 2021), (c) Ganzhi (Hu *et al.* 2015), (d) Lujiawan (Chen *et al.* 2016), (e) Jingbian (Li *et al.* 2022a), (f) Yulin (Lu *et al.* 2013), (g) Luochuan (Hu *et al.* 2015), (h) Jingchuan (Dong *et al.* 2015), (i) Yaoxian (Dong *et al.* 2015) and (j) Weinan (Kang *et al.* 2011). Red, blue and orange lines show the maximum values of χ_{LF} are in early Holocene, middle Holocene and late Holocene, respectively. The Luochuan and Ganzhi sections show the χ_{LF} from the Late Glacial and Holocene, respectively, controlled by an age, and they are assumed to have stable sedimentary rates.

for the lack of precise correspondence of climatic proxies from different sections in China and in the other parts of Asia. The Chinese Loess Plateau is both a sedimentary area and an erosion area (Xiong *et al.* 2023), and its aeolian deposition was possibly discontinuous at 2-ka scale (Zhu *et al.* 2007) at some places. This not only leads to incomplete sedimentary records, but also brings about chronology problems (Dong *et al.* 2015). Spatiotemporal change in source areas may also lead to non-correspondence in proxies (Xiong *et al.* 2023). Loess is indeed an excellent carrier of climate change and is more stable than fluviolacustrine deposits, and a section with high sedimentation rate, continuous deposits and excellent dating

materials is ideal for climate change studies. At all events, a reliable high-resolution chronology is the most important base, and the Minle section with 30 ^{14}C ages is clearly an excellent sedimentary record (Fig. 2, Zhong *et al.* 2022).

6 CONCLUSIONS

We analysed the mineral magnetic record from the Minle section in the Asian Monsoon marginal zone. SIRM and $\text{SIRM}_{\text{nmT}}/\text{SIRM}$ show a long-term variety of pedogenic magnetic mineral. We suggest that this long-term variation pattern is dominated by solar

insolation changes, which modulated the intensity of the Summer Monsoon and the Westerlies, the advance and retreat of the rain belt and local evapotranspiration. The Minle section is highlighted with the strongest pedogenesis and magnetic enhancement in the early Holocene within the past 13.3 ka, whose intensity is even stronger than the records of the Chinese Loess Plateau. We attribute this climatic optimum to the wettest climate in response to a combination of the strongest Asian Summer Monsoon and the weakest Westerlies, modulated by the highest summer insolation during the Holocene. After discussing the spatiotemporal differences in climatic records of the Chinese loess, we highlighted the importance of the Minle section.

SUPPORTING INFORMATION

Supplementary data are available at *GJI* online.

Figure S1. First-derivative curves of 42 samples from the Minle Section based on the DRS analysis.

Figure S2. I_{Hm} (content of haematite) and I_{Gt} (content of goethite) calculated from second derivative curve of one representative sample (~9.4 kyr) from PS8 based on the DRS data.

ACKNOWLEDGMENTS

All the measurements were undertaken in the Palaeomagnetism and Geochronology Laboratory, Institute of Geology and Geophysics, Chinese Academy of Sciences. This research was jointly financed by the National Natural Science Foundation of China (grant nos 42225205 and 41888101), the Second Tibetan Plateau Scientific Expedition and Research Program (grant 2019QZKK0704) and the Guangdong Province Introduced Innovative R&D Team of Geological Processes and Natural Disasters around the South China Sea (2016ZT06N331). YZ is supported by China Scholarship Council. Prof Yang Jingchun are highly appreciated for his very constructive comments on this manuscript. Dr Pengxiang Hu is thanked for her generous provision of the magnetic susceptibility data of the Ganzi section. Prof Zhaoxia Jiang, Dr Yunpeng Bi, Dr Xiu Hu, Hao Xie and Yifan Yao are thanked for their laboratory assistance. Our editors, Eduard Petrovsky and Andrew Biggin, and the reviewers, Junhuai Yang and Christian Zeeden are all enthusiastic and positive in pushing us to improve. They are especially thanked for their effort.

DATA AVAILABILITY

Original data collected for this paper (Data of ARM-SIRM and of DRS), Magnetic susceptibility data for Fig. 10, and extended figures can be found in the Supporting Information.

CONFLICT OF INTEREST

The authors declare no competing interests.

REFERENCES

- An, Z., et al., 2012. Interplay between the Westerlies and Asian monsoon recorded in Lake Qinghai sediments since 32 ka, *Sci. Rep.*, **2**, 1–7.
- An, Z., Kutzbach, J.E., Prell, W.L. & Porter, S.C., 2001. Evolution of Asian monsoons and phased uplift of the Himalaya–Tibetan plateau since late Miocene times, *Nature*, **411**(6833), 62–66.
- An, Z., Porter, S.C., Kutzbach, J.E., Xihao, W., Suming, W., Xiaodong, L. & Weijian, Z., 2000. Asynchronous Holocene optimum of the East Asian monsoon, *Quat. Sci. Rev.*, **19**(8), 743–762.
- Barrón, V. & Torrent, J., 2002. Evidence for a simple pathway to maghemite in Earth and Mars soils, *Geochim. cosmochim. Acta.*, **66**(15), 2801–2806.
- Berger, A. & Loutre, M.F., 1991. Insolation values for the climate of the last 10 million of years, *Quat. Sci. Rev.*, **10**, 297–317.
- Chen, F., Jia, J., Chen, J., Li, G., Zhang, X., Xie, H. & An, C., 2016. A persistent Holocene wetting trend in arid central Asia, with wettest conditions in the late Holocene, revealed by multi-proxy analyses of loess-paleosol sequences in Xinjiang, *China. Quater. Sci. Rev.*, **146**, 134–146.
- Chen, F.H. et al., 2010. Moisture changes over the last millennium in arid central Asia: a review, synthesis and comparison with monsoon region, *Quat. Sci. Rev.*, **29**(7–8), 1055–1068.
- Chen, F.H., Cheng, B., Zhao, Y., Zhu, Y. & Madsen, D.B., 2006. Holocene environmental change inferred from a high-resolution pollen record, Lake Zhuyeze, arid China, *Holocene*, **16**(5), 675–684.
- Day, R., Fuller, M. & Schmidt, V.A., 1977. Hysteresis properties of titanomagnetites: grain-size and compositional dependence, *Phys. Earth planet. Inter.*, **13**(4), 260–267.
- Deaton, B.C. & Balsam, W.L., 1991. Visible spectroscopy: a rapid method for determining hematite and goethite concentration in geological materials, *J. Sediment. Res.*, **61**, 628–632.
- Deng, C., Shaw, J., Liu, Q., Pan, Y. & Zhu, R., 2006. Mineral magnetic variation of the Jingbian loess/paleosol sequence in the northern Loess Plateau of China: implications for quaternary development of Asian aridification and cooling, *Earth planet. Sci. Lett.*, **241**(1–2), 248–259.
- Deng, C., Vidic, N.J., Verosub, K.L., Singer, M.J., Liu, Q., Shaw, J. & Zhu, R., 2005. Mineral magnetic variation of the Jiaodao Chinese loess/paleosol sequence and its bearing on long-term climatic variability, *J. geophys. Res.: Solid Earth*, **110**(B3). doi: 10.1029/2004JB003451.
- Dong, Y., Wu, N., Li, F., Huang, L. & Wen, W., 2015. Time-transgressive nature of the magnetic susceptibility record across the Chinese Loess Plateau at the pleistocene/holocene transition, *PLoS One*, **10**(7), e0133541.
- Dunlop, D.J., 2002. Theory and application of the day plot (Mrs/Ms versus Hcr/Hc) 1. Theoretical curves and tests using titanomagnetite data, *J. geophys. Res.: Solid Earth*, **107**(B3), EPM-4.
- Dunlop, D.J., Xu, S. & Franz, H., 2004. Alternating field demagnetization, single-domain-like memory, and the Lowrie-Fuller test of multidomain magnetite grains (0.6–356 μm), *J. geophys. Res. Atmos.*, **109**(B7), B07102.
- Forster, T. & Heller, F., 1997. Magnetic enhancement paths in loess sediments from Tajikistan, China and Hungary, *Geophys. Res. Lett.*, **24**(24), 17–20.
- Ganopolski, A., Kubatzki, C., Claussen, M., Brovkin, V. & Petoukhov, V., 1998. The influence of vegetation-atmosphere–ocean interaction on climate during the mid-holocene, *Science*, **280**, 1916–1919.
- Gao, F., Yang, J., Wang, S., Wang, Y., Li, K., Wang, F. & Xia, D., 2022. Variation of the winter mid-latitude westerlies in the Northern Hemisphere during the holocene revealed by aeolian deposits in the southern Tibetan Plateau, *Quat. Res.*, **107**, 104–112.
- Gao, X. et al., 2019. New high-temperature dependence of magnetic susceptibility-based climofunction for quantifying paleoprecipitation from Chinese loess, *Geochem. Geophys. Geosyst.*, **20**(8), 4273–4291.
- Guo, Z.T. et al., 2002. Onset of Asian desertification by 22 myr ago inferred from loess deposits in China, *Nature*, **416**, 159–163.
- Hartmann, K. & Wünnemann, B., 2009. Hydrological changes and Holocene climate variations in NW China, inferred from lake sediments of Juyanze palaeolake by factor analyses[J], *Quat. Int.*, **194**(1), 28–44.
- He, Y., Theakstone, W.H., Zhonglin, Z., Dian, Z., Tandong, Y., Tuo, C. & Hongxi, P., 2004. Asynchronous Holocene climatic change across China, *Quat. Res.*, **61**(1), 52–63.
- Heller, F. & Liu, T., 1984. Magnetism of Chinese loess deposits, *Geophys. J. Int.*, **77**(1), 125–141.
- Herzschuh, U., 2006. Palaeo-moisture evolution in monsoonal Central Asia during the last 50,000 years, *Quat. Sci. Rev.*, **25**(1–2), 163–178.

- Herzschuh, U., Tarasov, P., Wünnemann, B. & Kai, H., 2004. Holocene vegetation and climate of the Alashan Plateau, NW China, reconstructed from pollen data, *Palaeogeog. Palaeoclimat. Palaeoecol.*, **211**(1-2), 1–17.
- Hu, P., Liu, Q., Heslop, D., Roberts, A.P. & Jin, C., 2015. Soil moisture balance and magnetic enhancement in loess–paleosol sequences from the Tibetan Plateau and Chinese Loess Plateau, *Earth planet. Sci. Lett.*, **409**, 120–132.
- Jiang, N., Yan, Q., Xu, Z., Shi, J. & Zhang, R., 2020. The meridional shift of the midlatitude westerlies over arid central Asia during the past 21 000 years based on the TraCE-21ka simulations, *J. Clim.*, **33**, 7455–7478.
- Jiang, Z., Liu, Q., Roberts, A.P., Dekkers, M.J., Barrón, V., Torrent, J. & Li, S., 2022. The magnetic and color reflectance properties of hematite: from Earth to Mars, *Rev. Geophys.*, **60**(1), e2020RG000698.
- Kang, S., Lu, Y. & Wang, X., 2011. Closely-spaced recuperated OSL dating of the last interglacial paleosol in the southeastern margin of the Chinese Loess Plateau, *Quat. Geochronol.*, **6**(5), 480–490.
- Laskar, J., Robutel, P., Joutel, F., Gastineau, M., Correia, A.C. & Levrard, B., 2004. A long-term numerical solution for the insolation quantities of the Earth, *Astron. Astrophys.*, **428**(1), 261–285.
- Lattard, D., Engelmann, R., Kontny, A. & Sauerzapf, U., 2006. Curie temperatures of synthetic titanomagnetites in the Fe-Ti-O system: effects of composition, crystal chemistry, and thermomagnetic methods, *J. geophys. Res.: Solid Earth*, **111**(B12). doi: 10.1029/2006JB004591.
- Li, M., Hinnov, L.A. & Kump, L.R., 2019. Acycle: time-series analysis software for paleoclimate projects and education, *Comput. Geosci.*, **127**, 12–22.
- Li, P., Zhang, C., Wu, H. & Gao, Z., 2022a. Geochemical characteristics of Holocene loess-paleosol sequences in central Chinese Loess Plateau and their implications for East Asian monsoon evolution, *Quat. Int.*, **616**, 99–108.
- Li, Y., Wang, N., Cheng, H., Long, H. & Zhao, Q., 2009a. Holocene environmental change in the marginal area of the Asian monsoon: a record from Zhuye Lake, NW China, *Boreas*, **38**(2), 349–361.
- Li, Y., Wang, N., Morrill, C., Cheng, H., Long, H. & Zhao, Q., 2009b. Environmental change implied by the relationship between pollen assemblages and grain-size in N.W. Chinese lake sediments since the Late glacial, *Rev. Palaeobot. Palynol.*, **154**(1), 54–64.
- Li, Z., Sheng, M., Wang, X., Jiang, K., Sun, P., Yi, S. & Yang, Z., 2022b. Irreversible intensification of the East Asian winter monsoon and aridity in Asian interior linked to the uplifted Tibetan Plateau: evidence from magnetoclimatology of the Xining loess since 1.3 ma, *Quat. Sci. Rev.*, **298**, 107875.
- Liang, X., Yang, P., Yao, J., Zhang, P., Zhang, J., Sun, P. & Ao, H., 2021. Environmental magnetic record of East Asian summer monsoon variability on the Chinese Loess Plateau since 16 ka BP, *Acta Geogr. Sin.*, **76**(3), 539–549 (in Chinese).
- Liu, C., Wang, W. & Deng, C., 2020. A new weathering indicator from high-temperature magnetic susceptibility measurements in an Argon atmosphere, *Geophys. J. Int.*, **221**(3), 2010–2025.
- Liu, Q. *et al.*, 2004. Mechanism of the magnetic susceptibility enhancements of the Chinese loess, *J. geophys. Res.: Solid Earth*, **109**. doi: 10.1029/2004JB003249.
- Liu, Q., Deng, C., Torrent, J. & Zhu, R., 2007. Review of recent developments in mineral magnetism of the Chinese loess, *Quat. Sci. Rev.*, **26**(3-4), 368–385.
- Liu, Q., Deng, C., Yu, Y., Torrent, J., Jackson, M.J., Banerjee, S.K. & Zhu, R., 2005. Temperature dependence of magnetic susceptibility in an argon environment: implications for pedogenesis of Chinese loess/paleosols, *Geophys. J. Int.*, **161**(1), 102–112.
- Long, H., Lai, Z.P., Fuchs, M., Zhang, J.R. & Yu, L., 2012. Timing of late quaternary palaeolake evolution in Tengger Desert of northern China and its possible forcing mechanisms, *Global planet. Change*, **92–93**(4), 119–129.
- Long, H., Lai, Z.P., Wang, N.A. & Li, Y., 2010. Holocene climate variations from Zhuyeze terminal lake records in East Asian monsoon margin in arid northern China, *Quat. Res.*, **74**(74), 46–56.
- Lu, H., Yi, S., Liu, Z., Mason, J.A., Jiang, D., Cheng, J. & Otto-Bliesner, B., 2013. Variation of East Asian monsoon precipitation during the past 21 ky and potential CO2 forcing, *Geology*, **41**(9), 1023–1026.
- Maher, B.A., 1988. Magnetic properties of some synthetic sub-micron magnetites, *Geophys. J. Int.*, **94**(1), 83–96.
- Maher, B.A., 1998. Magnetic properties of modern soils and quaternary loessic paleosols: paleoclimatic implications, *Palaeogeog. Palaeoclimat. Palaeoecol.*, **137**(1-2), 25–54.
- Maher, B.A. & Thompson, R., 1992. Paleoclimatic significance of the mineral magnetic record of the Chinese loess and paleosols, *Quat. Res.*, **37**(2), 155–170.
- Mullins, C.E., 1977. Magnetic susceptibility of the soil and its significance in soil science—a review, *J. Soil Sci.*, **28**(2), 223–246.
- Orgeira, M.J., Egli, R. & Compagnucci, R.H., 2011. A quantitative model of magnetic enhancement in loessic soils, In: Petrovský, E., Ivers, D., Hari-narayana, T. & Herrero-Bervera, E. (Eds.), *The Earth's Magnetic Interior*. Springer, Netherlands, pp. 361–397.
- Ran, M. & Feng, Z., 2013. Holocene moisture variations across China and driving mechanisms: a synthesis of climatic records, *Quat. Int.*, **313**, 179–193.
- Rao, Z., Wu, D., Shi, F., Guo, H., Cao, J. & Chen, F., 2019. Reconciling the ‘westerlies’ and ‘monsoon’ models: a new hypothesis for the Holocene moisture evolution of the Xinjiang region, NW China, *Earth Sci. Rev.*, **191**, 263–272.
- Roberts, A.P., Liu, Q., Rowan, C.J., Chang, L., Carvallo, C., Torrent, J. & Horng, C.S., 2006. Characterization of hematite (α -Fe₂O₃), goethite (α -FeOOH), greigite (Fe₃S₄), and pyrrhotite (Fe₇S₈) using first-order reversal curve diagrams, *J. geophys. Res.: Solid Earth*, **111**(B12). doi: 10.1029/2006JB004715.
- Roberts, A.P., Pike, C.R. & Verosub, K.L., 2000. First-order reversal curve diagrams: a new tool for characterizing the magnetic properties of natural samples, *J. geophys. Res.: Solid Earth*, **105**(B12), 28461–28475.
- Smirnov, A.V., 2006. Low-temperature magnetic properties of magnetite using first-order reversal curve analysis: implications for the pseudo-single-domain state, *Geochem. Geophys. Geosyst.*, **7**(11). doi: 10.1029/2006GC001397.
- Tang, M.C., Shen, Z.B. & Chen, Y.Y., 1979. On climatic characteristics of the Xizang Plateau monsoon, *Acta Geogr. Sin.*, **34**(1), 34–41 (in Chinese).
- Torrent, J. & Barron, V., 2008. Diffuse reflectance spectroscopy, In: Ulery, A. L. & Dress, R. eds. *Methods of Soil Analysis Part 5: Mineralogical Methods*. Madison, Wisconsin, USA: Soil Science Society of America, Inc., pp. 367–387.
- Trouet, V., Esper, J., Graham, N.E., Baker, A., Scourse, J.D. & Frank, D.C., 2009. Persistent positive North Atlantic oscillation mode dominated the medieval Climate anomaly, *Science*, **324**(5923), 78–80.
- Wünnemann, B., Kai, H., Janssen, M. & Hucai, C.Z., 2007. Responses of Chinese desert lakes to climate instability during the past 45,000 years, *Develop. Quater. Sci.*, **9**(07), 11–24.
- Xiong, J., Wang, Y., Picotti, V., Zhang, H., Liu, Q., Zhao, X. & Zhang, P., 2023. Proximal supply in loess deposition of the Chinese Loess Plateau, *J. geophys. Res.: Earth Surf.*, **128**(3), e2022JF006814.
- Yan, M., Liu, Z.Y., Ning, L. & Liu, J., 2020. Holocene EASM-EAWM relationship across different timescales in CCSM3, *Geophys. Res. Lett.*, **47**. doi: 10.1029/2020GL088451.
- Yang, S., Chen, Z., Chen, H., Luo, Y., Liu, L., Liu, X. & Li, P., 2022. Magnetic properties of the Ganzi loess and their implications for precipitation history in the eastern Tibetan Plateau since the last interglacial, *Paleocean. Paleoclimat.*, **37**(2), e2021PA004322.
- Yu, Y. *et al.*, 2006. Millennial-scale Holocene climate variability in the NW China drylands and links to the tropical Pacific and the North Atlantic, *Palaeogeog. Palaeoclimat. Palaeoecol.*, **233**(1), 149–162.
- Zhang, C. & Li, Y., 2016. Verification of watershed vegetation restoration policies, arid China, *Sci. Rep.*, **6**(1), 30740. doi: 10.1038/srep30740.
- Zhang, H. *et al.*, 2021a. A data-model comparison pinpoints holocene spatiotemporal pattern of East Asian summer monsoon, *Quat. Sci. Rev.*, **261**, 106911, doi: 10.1016/j.quascirev.2021.106911.

- Zhang, Z., Liu, J., Chen, J., Chen, S., Shen, Z., Liu, X. & Chen, F., 2021b. Holocene climatic optimum in the East Asian monsoon region of China defined by climatic stability, *Earth Sci. Rev.*, **212**, 103450.
- Zhao, Y. & Yu, Z., 2012. Vegetation response to Holocene climate change in East Asian monsoon-margin region, *Earth Sci. Rev.*, **113**(1–2), 1–10.
- Zhong, Y. et al., 2022. Jet transitions caused multiple abrupt droughts in the Asian summer monsoon margin during Holocene times, *Palaeogeog. Palaeoclimat. Palaeoecol.*, **601**(2022), 111106.
- Zhou, L., Oldfield, F., Wintle, A.G., Robinson, S.G. & Wang, J., 1990. Partly pedogenic origin of magnetic variations in Chinese loess, *Nature*, **346**(6286), 737–739.
- Zhu, R., Zhang, R., Deng, C., Pan, Y., Liu, Q. & Sun, Y., 2007. Are Chinese loess deposits essentially continuous?, *Geophys. Res. Lett.*, **34**(17). doi: 10.1029/2007GL030591 .